Title: Observation-constrained multicycle dynamic models of the Pingding Shan earthquake gate along the Altyn Tagh Fault

Dunyu Liu[1,*], Benchun Duan[1], Veronica B. Prush[2,**], Michael E. Oskin[2] and Jing Liu-Zeng[3]

[1] Center for Tectonophysics, Department of Geology & Geophysics, Texas A&M University, College Station, TX, 77843-3115, USA.

[2] Department of Earth and Planetary Sciences, University of California, Davis, 1 Shields Avenue, Davis, CA, 95616, USA.

[3] Institute of Surface-Earth System Science, Tianjin University, Tianjin, 300072, China.

*Corresponding author: dliu@ig.utexas.edu. Now at University of Texas Institute for Geophysics, 10601 Exploration Way, Austin, TX, 78758, USA.

** Now at Department of Earth and Planetary Sciences, McGill University, 3450 University Street, Montréal, Quebec, H3A 0E8, Canada.

Prepared for Publication in Tectonophysics

First submitted on September 22, 2020

Revision submitted on April 06, 2021

Abstract:

Earthquake gates are fault geometric complexities, common in natural fault systems, that conditionally impede earthquake ruptures. This study centers on modeling of multicycle dynamics of the Pingding Shan earthquake gate along the central Altyn Tagh Fault in northwest China. The earthquake gate includes three geometric complexities: a prominent restraining bend, a 4-km wide stepover to the east, and a releasing bend to the west. We use a 2D finite element method to simulate coseismic spontaneous ruptures with interseismic fault stress evolutions computed by an analytic viscoelastic solution. Paleoseismic records and long-term slip-rates are used to constrain the models. We find that fault-geometry-related heterogenous stresses accumulated over earthquake cycles yield complex rupture patterns and help explain earthquake recurrence intervals revealed by paleoseismic records. The three most important contributions to the heterogeneous stresses come from dynamic ruptures passing fault geometric complexities, fault-strike-dependent tectonic loading and relaxation, and stress history from past earthquakes. In the Pingding Shan earthquake gate, the releasing stepover appears to impede ruptures more effectively than the restraining bend. The combined impact of the restraining bend and the releasing stepover makes the Pingding Shan earthquake gate a very effective barrier to 350-km model-spanning ruptures. The best-fit model yields a low recurrence interval of 4.6 kyrs for 350-km-long ruptures, interspersed with more frequent ruptures limited to individual fault segments. A lower static friction tends to reduce the effectiveness of the earthquake gate to impede ruptures. Local fault geometric complexities together with rapid energy release and restrengthening of friction during dynamic ruptures help explain the 0.66 recurrence interval coefficient of variation (COV) recorded at the Copper Mine paleoseismic trench site on the Xorxoli segment. This study provides a method for applying heterogenous initial stresses for single-event dynamic rupture simulations that consider the effect of past earthquakes and fault geometry.

Key words: Dynamic rupture, fault geometric complexity, earthquake cycle, earthquake gate, stress heterogeneity, Altyn Tagh fault

1 Introduction

Fault geometric complexities, such as fault bends and stepovers, are common in natural fault systems, and earthquake ruptures often stop at these complexities (e.g., King and Nabelek, 1985; Sibson, 1985; Wesnousky, 1988). However, some recent earthquakes, such as the 1992 M_w 7.3 Landers (California) earthquake (e.g., Massonnet et al., 1993; Cohee and Beroza, 1994; Olsen, 1997) and the 2016 M_w 7.8 Kaikoura (New Zealand) earthquake (e.g., Hamling et al., 2017; Kaiser et al., 2017; Ulrich et al., 2019), break through these geometric complexities. These fault complexities can be conceptualized as "earthquake gates" (Oskin et al., 2015; Duan et al., 2019), which means that they may be closed (i.e., dynamic ruptures stop at these locations) in some earthquakes while open (i.e., dynamic ruptures propagate through them) in others, depending on fault geometry and prior rupture history. Assessing the likelihood and conditions under which earthquake gates are open, leading to multi-fault and multi-segment ruptures and thus larger earthquakes, are important questions in the earthquake science and seismic hazard analysis communities.

Geologic observations of mapped historic earthquakes give us first-hand data on the likelihood of fault geometric complexities to impede rupture propagation (Wesnousky, 2006; Biasi and Wesnousky, 2016, 2017). Wesnousky (2006) and Biasi and Wesnousky (2016) find that two-thirds of strike-slip ruptures terminate at stepovers or fault tips and that the likelihood of a rupture jumping past a stepover decreases with increasing stepover offset. Similarly, the likelihood of a rupture passing a fault bend decreases with increasing bend angles (Biasi and Wesnousky, 2017). In addition, Elliott et al. (2009) and Oglesby (2008) show that ruptures may breach a stepover when the coseismic slip gradient near the stepover is greater than 20 cm/km. However, these empirical relations are drawn on limited observations. This was demonstrated by the 2016 M_w 7.8 Kaikoura earthquake, whose complex rupture breaks at least 13 fault segments and jumps across gaps as wide as 20 km (e.g., Kaiser et al., 2017) and the 1992 M_w 7.3 Landers earthquake that breaks multiple fault segments (e.g., Cohee and Beroza, 1994).

Spontaneously dynamic rupture models are used to test the mechanical conditions behind empirical geologic observations and evaluate the likelihood of dynamic ruptures terminating or breaking through fault geometric complexities. These models shed light on how fault geometric measurements and mechanical properties, such as stepover offset, bend angle or branch angle, fault roughness, friction laws, and prestress conditions, affect dynamics of ruptures propagating through geometric complexities (e.g., Harris and Day, 1993; Dunham et al., 2011b; Lozos et al., 2011; Ryan and Oglesby, 2014; Luo and Duan, 2018). For example, Harris and Day (1993) show that a strike-slip rupture is unlikely to jump a stepover wider than 5 km, and dynamically propagating ruptures can jump both compressional and dilatational stepovers. Ryan and Oglesby (2014) test how different friction laws, including the slip-weakening law (e.g., Andrews, 1976) and three forms of rate- and state-dependent friction (e.g., Ruina, 1983), affect whether a rupture can jump a stepover. They find that the functional forms of various friction laws have a secondary effect if the friction laws are scaled to give comparable fracture energy. Fault geometric complexities and prestresses also affect rupture directivity. Oglesby and Mai (2012) develop 3D dynamic rupture models of earthquakes on the North Anatolian Fault system, Turkey. They find that a rupture may propagate through the entire fault system if it nucleates far from an oblique normal fault stepover segment while a rupture may die out in the stepover if it nucleates near the stepover. They also find that the pattern can change drastically when the prestress field is rotated by only 10°. A limitation of these single-event dynamic models, however, is that initial stress conditions are typically resolved from a uniform regional stress field according to local fault strike, which does not account for rupture history and stress heterogeneity inherited from past earthquakes.

Multicycle dynamic models, which place dynamic ruptures in the context of earthquake cycles and thus take into account the effects of past earthquakes on initial stress conditions of dynamic ruptures, demonstrate that stress heterogeneity near fault geometric complexities plays a critical role in impeding or passing dynamically propagating ruptures (Duan and Oglesby, 2005, 2006, 2007; Liu et al., 2020). Contributions to stress heterogeneity come from dynamic ruptures through geometric complexities, strike-dependent tectonic loading and relaxation, and the residual stress from past earthquakes. For example, Liu et al. (2020) use a three-dimensional finite element earthquake simulator EQsimu to model fully dynamic earthquake cycles on a bent fault governed by rate- and state-dependent friction. They demonstrate that the zone of stress heterogeneity near the fault bend will widen and complex rupture patterns develop over multiple earthquake cycles on a bent fault.

An important step forward is to apply these multicycle dynamic models to real fault systems. The 1500 km-long active Altyn Tagh Fault (ATF) in northwest China is a natural laboratory to study earthquake gate behaviors. The ATF, a left-lateral strike-slip fault, is the major lithospheric boundary between the Tarim Basin to the north and the Tibetan Plateau to the south (e.g., Molnar and Tapponnier, 1978). In addition, there are four major earthquake gates along the central ATF, including the Aksay, Pingding Shan, Akato Tagh, and Sulamu Tagh double bends from east to west (see Figure 1 for the first three). Previously, Duan et al. (2019) apply a multicycle dynamic model to the Aksay double restraining bend of the ATF. They find that the Aksay bend is an effective barrier to dynamically propagating ruptures from either side of the bend within a wide range of parameters. However, roughly 10% of ruptures jump across the bend to break the entire modeled fault system. They also find that secondary complexities in fault geometry within the Aksay bend, especially those aligned with the regional strike of the fault system, play a critical role in permitting the occasional jumping ruptures. In this study, we examine rupture behavior at the Pingding Shan earthquake gate, which includes a prominent restraining bend, a 4-km wide stepover to the east, and a releasing bend to the west. This earthquake gate is bounded by the Wuzhunxiao segment to the west and the Xorxoli segment to the east (Figure 1). We will make use of available paleoseismic, geologic, and geodetic data to build observation-constrained multicycle dynamic models of this earthquake gate.

The coefficient of variation (COV) of recurrence intervals at a paleoseismic trench site has been used to characterize the complexity of earthquake recurrence in a fault system (e.g., Scharer et al., 2010; Williams et al., 2019). COV is calculated by dividing the standard deviation of recurrence intervals by their mean. A COV near zero indicates periodic to quasi-periodic earthquake recurrence. A COV of one describes a random, uncorrelated recurrence. A COV greater than one suggests clustered earthquake recurrence. The Copper Mine paleoseismic trench site to the east of the Pingding Shan earthquake gate is located on the Xorxoli segment of the ATF (Figure 1). Yuan et al. (2018) identify nine earthquakes over the past 6000 years at the site, with a recurrence interval of 624±411 years and a COV of 0.66. COVs are still rarely used to constrain numerical models but reproducing observed COVs with multicycle dynamic models would be critical to the models' credibility to capture complex dynamics in a fault system.

Slip rates along the ATF have been estimated from both geodetic and geologic observations (Table S1 in the supplementary material). Regional GPS network data collected from 1993 to 1998 conclude a slip rate ~9 mm/yr for the ATF (Shen et al., 2001). For a 300-km-long profile between 88˚E and 91˚E, Bendick et al. (2000) and Wallace et al. (2004) determine a slip rate of 9±5 mm/yr based on GPS measurements. At 85°E, InSAR data yields a slip rate of 11±5 mm/yr, assuming no relative vertical motion and a 15-km locking depth (Elliott et al., 2008). At 94°E, Jolivet et al. (2008) determine slip rate of 8~10 mm/yr with InSAR data, assuming a locking depth of 7-9 km using a thin-plate model sheared at its base. Geologic studies concur with geodetic analyses, suggesting a long-term slip rate of 9±2 mm/yr since the initiation of the ATF aged 49 Ma (Yin et al., 2002) and an upper bound of 10 mm/yr for post-Early Miocene slip (Yue et al., 2004). Although fast Quaternary slip rates of 26.9±6.9 mm/yr are obtained at Cherchen He and Sulamu Tagh near 86.6°E based on fluvial and glacial geomorphic markers (Mériaux et al., 2004), these rates are suspected to be too fast due to assumptions in offset construction (Cowgill, 2007). Cowgill (2007) revises the rate down to ~9 mm/yr at Cherchen He. Cowgill et al. (2009) determine a Quaternary slip rate of 9-14 mm/yr by tightly bracketing the age of a displaced fluvial terrace riser at Yuemake (88.51°E). Elliott (2014) revises the slip rate at the Huermo Bulak He site on the eastern northern strand of ATF down to 6.3+2.1/-1.6 mm/yr, which is substantially lower than some earlier estimates but agrees with rates from geodetic models and older offset geomorphic markers. Within the Pingding Shan earthquake gate, Mériaux et al. (2012) conclude that the slip rate of the ATF is 13.9±1.1 mm/yr at two sites located at ~90.5°E. More recently, Prush et al. (personal communications) has revised this slip rate to 4.7±0.8 mm/yr. This latter slip rate estimate will be used in this study to constrain our model parameters. In addition to paleoseismic and slip rate observations of ATF, we also constrain our models using slip-per-event estimates. Geomorphic offsets show maximum surface displacement (slip-per-event) by the most recent earthquakes are 4-7 meters between 90.0°E and 91.5°E (Washburn et al., 2001) and are 3-8 m for the Aksay bend at about 94°E

(Elliott et al., 2015).

In this study, we integrate paleoseismic records, geodetic, and geologic observations with multicycle dynamic models to study rupture behavior of the Pingding Shan earthquake gate over multiple earthquake cycles. We investigate the conditions for system-spanning ruptures that break the gate and assess their probability. We first briefly review the 2D multicycle dynamic modeling method. Then we describe the fault geometry and parameters of the finite element models. We present results from the model that can best fit paleoseismic records, slip rate estimates, and slip-per-event observations. Finally, key parameters that influence earthquake multicycle dynamics are explored, and remaining issues are further discussed.

2 Methods

We apply a dynamic finite element code, EQdyna (Duan and Oglesby, 2006), to simulate the coseismic dynamic rupture process for each event over multiple earthquake cycles. EQdyna has been tested in the SCEC/USGS dynamic code verification exercise and performs well (Harris et al., 2009; Harris et al., 2018). In each interseismic period, we use a linear Maxwell viscoelastic model with an analytical solution to calculate fault stress evolution on geometrically complex faults (Nielsen and Knopoff, 1998; Duan and Oglesby, 2005). The model consists of an elastic spring and a viscous dashpot in series (Jaeger, 1969) with the stress-strain relations written as

$$\sigma = \sigma_e = \sigma_v, \qquad (1)$$

$$\varepsilon = \varepsilon_e + \varepsilon_v, \qquad (2)$$

where σ and ε are stress and strain, respectively, and subscript e stands for elastic component while v represents the viscous component. Assuming pure shear loading, the constitutive relations can be expressed as

$$\sigma_e = \mu\varepsilon_e, \qquad (3)$$

$$\sigma_v = \eta\dot{\varepsilon}_v, \qquad (4)$$

where μ is the shear modulus, η is the viscosity, and the overdot denotes time derivative.

Equations (1)-(4) lead to the constitutive relation for the Maxwell viscoelastic model as

$$\frac{\sigma}{\mu} + \frac{\dot{\sigma}}{\eta} = \dot{\varepsilon}\,. \tag{5}$$

Assuming the strain rate $\dot{\varepsilon}$ is a constant over each interseismic period, we can solve the equation (5) for the stress and resolve it onto the shear and normal directions of a fault segment. The shear stress $\sigma_\tau(t)$ and the normal stress $\sigma_n(t)$ on a fault segment at time t, which is the elapsed time since last earthquake, can be written as

$$\sigma_\tau(t) = (\sigma_\tau^0 - \eta\gamma_\tau)\exp\left(-\frac{\mu}{\eta}t\right) + \eta\gamma_\tau, \tag{6}$$

$$\sigma_n(t) = (\sigma_n^0 - \eta\gamma_n)\exp\left(-\frac{\mu}{\eta}t\right) + \eta\gamma_n, \tag{7}$$

$$\gamma_\tau = \gamma\cos(2\phi), \qquad \gamma_n = \gamma\sin(2\phi)\,. \tag{8}$$

Here, $\sigma_\tau^0, \sigma_n^0$ are fault shear stress and normal stress at the beginning of the interseismic period (i.e., t=0), respectively. $\gamma_\tau, \gamma_n, \gamma$ and ϕ are fault shear strain rate, fault normal strain rate, maximum shear strain rate in the model, and the angle between the maximum shear loading direction and the local strike of a fault segment, respectively.

In addition to the tectonic loading, gravity also contributes to stresses on the fault. The model assumes the fault is buried at a certain depth and the equilibrium (ambient) normal stress resulting from the lithostatic stress is part of the total normal stress on the fault. This ambient normal stress, σ^a, is assumed to be not relaxed. Therefore, the total normal stress on a fault segment $\sigma_N(t)$ is

$$\sigma_N(t) = \sigma_n(t) + \sigma^a, \quad \sigma_N^0 = \sigma_n^0 + \sigma^a. \tag{9}$$

Substituting equation (9) into equation (7), the total normal stress during the interseismic period is

$$\sigma_N(t) = (\sigma_N^0 - \sigma^a - \eta\gamma_n)\exp\left(-\frac{\mu}{\eta}t\right) + \eta\gamma_n + \sigma^a. \tag{10}$$

The viscoelastic model accounts for the effects of off-fault deformation, such as secondary faulting, aftershocks, and topographic changes, on the fault shear and normal stresses at fault complexities to alleviate pathological fault behavior (e.g., permanently locking or fault opening) (Nielsen and Knopoff, 1998; Duan and Oglesby, 2005). This is a very simplified, approximate version of the interseismic phase of an earthquake cycle, but it captures the impacts of tectonic loading and stress relaxation on fault stress evolution between two consecutive earthquakes.

When a critical point on the fault system reaches failure level (i.e., the Mohr-Coulomb failure criterion) from the viscoelastic calculation, we run EQdyna for the coseismic dynamic rupture process with initial fault shear and normal stresses calculated from equations (6) and (10) by forcing the rupture to propagate at a speed of 1.5 km/s within 2 km of the failure point. After dynamic rupture spontaneously stops, the residual stress on the fault from the dynamic event will be used as the initial stress conditions for the next interseismic viscoelastic calculation, and fault friction will be reset to the static level. The process repeats as many times as needed to obtain multiple cycle results. Typically, we run a few thousand earthquake cycles for a model.

A slip-weakening friction law is typically used in spontaneous rupture simulations (e.g., Andrews, 1976; Day, 1982), in which fault friction decreases linearly with slip up to a threshold. The law works well for ground motion applications but does not include a slip rate dependence of friction. The rate dependence of friction has been observed in low-speed friction experiments (e.g., Dieterich, 1979; Ruina, 1983), and strongly rate-weakening friction laws are proposed based on high-speed friction experiments (e.g., Di Toro et al., 2004). In addition, rate-dependence of friction is shown to produce pulse-like ruptures inferred from seismic observations (Heaton, 1990) because of the healing effect at the end of sliding in this type of friction laws. In this study, we use a slip- and rate- weakening friction law (Duan, 2019) in the dynamic rupture process to control the friction evolution during dynamic events. The friction law follows:

$$f_1(d) = \begin{cases} f_s - \frac{(f_s - f_d)d}{d_0} & d \le d_0 \\ f_d & d > d_0 \end{cases}, \qquad (4a)$$

$$f_2(v) = \begin{cases} f_r - \frac{(f_r - f_d)v}{v_0} & v \le v_0 \\ f_d & v > v_0 \end{cases}, \qquad (4b)$$

$$f(d, v) = \max\big(f_1(d), f_2(v)\big), \qquad (4c)$$

where f_r is the restrengthening friction coefficient after the sliding stops. Its value is between the dynamic friction coefficient f_d and the static friction coefficient f_s. *d* and *v* are slip and slip velocity on the fault, respectively, and d_0 and v_0 are the critical slip distance and critical velocity, respectively. The friction law behaves like the classical slip-weakening law in the early phase of slip, with restrengthening of friction when the slip velocity drops below v_0 in the latter phase of slip. Similar slip- and rate-dependent friction laws have been used in other earlier studies (e.g., Madariaga et al., 1998; Aagaard et al., 2001)

3 Models

3.1 The fault geometry

The ATF geometry is inferred from field and remote mapping and prior publications (e.g., Washburn et al., 2001; Washburn et al., 2003; Cowgill et al., 2004; Mériaux et al., 2005; Cowgill et al., 2009; Gold et al., 2009; Mériaux et al., 2012; Elliott, 2014 ; Prush et al., personal communications). Figure 1 shows the trace (white dots) of the 350-km-long central Altyn Tagh Fault straddling the Pingding Shan earthquake gate. To focus on the effect of first order and macroscopic scale fault geometry on rupture dynamics along the fault system, we sample the fault (red dots) at 4-km intervals along strike. Within the vicinity of the Pingding Shan there are three main geometric complexities present: a 4-km releasing stepover in the east, a prominent restraining bend southwest to the Pingding Shan, and a large releasing bend in the west. The Akato Tagh and Aksay restraining double bends delimit the western and eastern ends of the model, respectively. The Wuzhunxiao, Pingding Shan and Xorxoli segments are indicated in Figure 1. In this model, we exclude the thrust faults north of the Pingding Shan and the normal fault within the stepover.

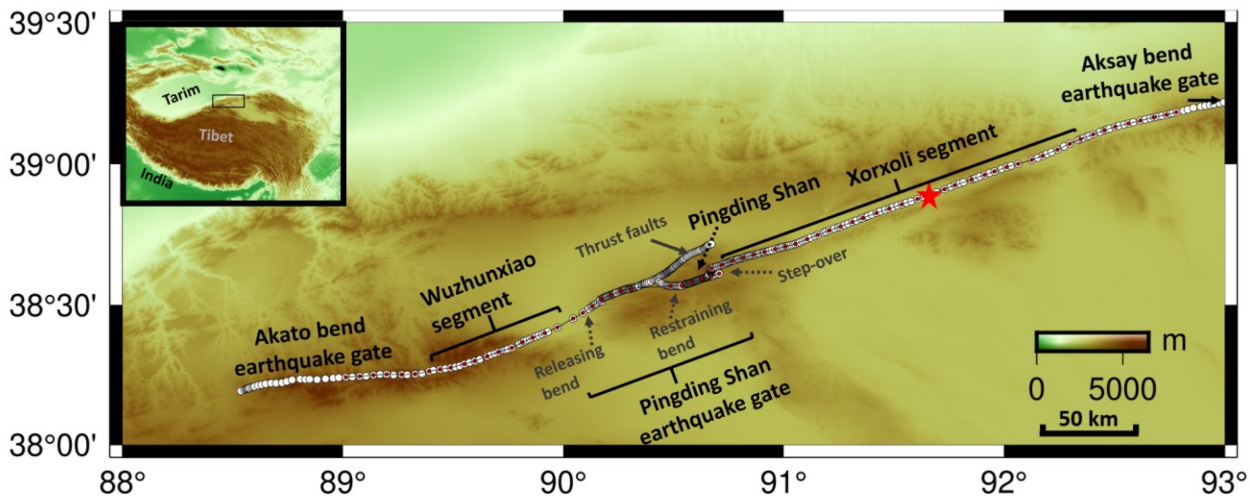

Figure 1. Fault geometry of the Pingding Shan earthquake gate of the central Altyn Tagh Fault. White dots indicate the mapped fault trace. The red dots are model control points sampled at 4-km intervals along strike of the fault system. The Pingding Shan earthquake gate includes a prominent restraining bend, a 4-km wide stepover to the east, and a releasing bend to the west. The gate is bounded by the Wuzhunxiao and Xorxoli segments to the west and east, respectively. Inset gives the tectonic setting and background of the studied region. Thrust faults north of the Pingding Shan are indicated but not included in the model. We focus mainly on the effect of the first order and macroscopic fault geometry on the dynamics of the fault system. The Copper Mine paleoseismic trench site (Yuan et al., 2018) is denoted by the red star.

3.2 Model Parameters

The complexity of earthquake phenomena can be attributed to heterogeneity in fault geometry, fault prestresess, friction, rock material properties and rheology, etc. In this study, we focus on the impact of the realistic fault geometry on rupture dynamics, keeping other model parameters uniform in each model. For different models we adjust 1) the static friction coefficient f_s, 2) the dynamic friction coefficient f_d, 3) the restrengthening friction coefficient f_r, 4) the critical slip velocity v_0, and 5) the viscosity η used for the tectonic loading and stress relaxation. In all models we assume homogeneous rock properties with $V_p = 6000\ \mathrm{m/s}$, $V_s = 3464\ \mathrm{m/s}$ and density $\rho = 2670\ \mathrm{kg/m^3}$. The maximum shear strain rate is $3.9 \times 10^{-15}/\mathrm{yr}$ based on a recent interferometric synthetic aperture radar study to the west (Zhu et al., 2016). We choose a time step of 1 yr for the interseismic loading. For dynamic ruptures the time step is $dt = \alpha dx/V_p$, where α is a constant between 0 and 1, dx is the element size and V_p is P-wave velocity. Given $dx = 200\ \mathrm{m}$, $V_p = 6000\ \mathrm{m/s}$, and $\alpha = 0.5$, $dt = 0.0167\ \mathrm{s}$. We conservatively choose $dt = 0.01\ \mathrm{s}$.

We choose an ambient normal stress (σ_a) of 100 MPa, which corresponds to the effective normal stress at about 6 km depth, assuming hydrostatic pore pressure. We note that after many earthquakes on this geometrically complex fault system, stresses on the fault become very heterogeneous. Although the viscoelastic model in this study intends to avoid fault opening at fault complexities that is considered to be nonphysical at the depth, we apply a lower bound of the absolute normal stress of 10 MPa to ensure that fault opening does not happen in the models. The viscosity has a minimum value $\eta_{min} = f_s\sigma_a/\gamma$ (Duan and Oglesby, 2005), below which earthquakes cannot nucleate in the models because the tectonic loading is effectively relaxed. η_{min} is 7.7×10^{21} Pa • s for a fault system with a low $f_s = 0.3$ and 2.2×10^{22} Pa • s for a fault system with a high $f_s = 0.7$.

Given an ambient stress field, f_s determines the overall shear strength of the fault system. This strength of the fault system affects the degree to which elastic strain energy accumulated near the fault is partitioned to earthquake slip or off-fault deformation, which is critical to fit the models to the long-term slip rate data. Given a specified initial stresses, f_d will determine the stress drop, which is the difference between the initial shear stress and the multiplication of normal stress and f_d. Note that the heterogeneity of on-fault stresses over many earthquake cycles on a realistic fault geometry leads to very heterogenous shear strength and stress drop distributions. Therefore, we frame our discussions of fault shear strength and stress drop in terms of f_s and f_d, respectively. We also test f_r and v_0 between models because a strong and rapid restrengthening process during dynamic ruptures may increase the heterogeneity of stress along the fault system, which is important to fit modeled earthquake recurrence to paleoseismic observations including COV.

To test the impact of various parameters on multicycle dynamics of the earthquake gate, we run eight models using the prescribed fault geometry (Table 1). Model A has a $f_s = 0.5$, $f_d = 0.43$, which yields an apparent stress drop of 7 MPa and $f_r = 0.49$. We also run 5 variations of Model A (Models A1-A5), in which one parameter value is different from that in Model A (Table 1). Model B represents a fault system with a higher shear strength of $f_s = 0.7$, typical of low-speed rock friction experiments (Byerlee, 1978). Model C represents a fault system with a lower shear strength of $f_s = 0.3$ following observations that mature strike-slip faults may be inherently weak (e.g., Rice, 1992; Dunham et al., 2011a). We run 2500 earthquake cycles for Model A and 1500 cycles for other models.

Table 1. Key parameters of models presented in this study. Changes of parameters relative to the reference Model A are bolded.

Models/ Parameters	Static friction f_s	Dynamic friction f_d	Restrenthe-ning friction f_v	Viscosity η (Pa s)	v_0 (m/s)	d_0 (m)
A	0.5	0.43	0.49	2.5×10^{22}	0.2	0.5
A1	0.5	**0.45**	0.49	2.5×10^{22}	0.2	0.5
A2	0.5	0.43	**0.47**	2.5×10^{22}	0.2	0.5
A3	0.5	0.43	0.49	2.5×10^{22}	**1.0**	0.5
A4	0.5	0.43	0.49	2.5×10^{22}	0.2	**1.0**
A5	0.5	0.43	0.49	$\mathbf{3.5 \times 10^{22}}$	0.2	0.5
B	**0.7**	**0.63**	**0.69**	2.5×10^{22}	0.2	0.5
C	**0.3**	**0.23**	**0.29**	2.5×10^{22}	0.2	0.5

4. Results

4.1 Best-fit Model A to observations and the statistics from Model A

Figure 2 (Top) compares long-term slip rates calculated from five models (Models A, A1, A5, B, and C). In Model A, the maximum long-term slip rate at the Wuzhunxiao, Pingding Shan, and Xorxoli segments are about 8.5, 5, and 12 mm/yr, respectively, which are indicated by red dots. Long-term slip rates vary along fault strikes and they decrease to zero when approaching fault tips. The long-term slip rates from Model A match the observed 9-14 mm/yr slip rate of the ATF of the region (e.g., Shen et al., 2001; Cowgill et al., 2009) and the recently revised low 4.7±0.8 mm/yr slip rate east of the Pingding Shan restraining bend (Prush et al., personal communications). Model B, which has a higher static friction coefficient of 0.7 (high shear strength), gives long-term slip rates less than half of Model A. Model C, which has a low static friction of 0.3 (low shear strength), produces slip rates that are about 4 mm/yr greater than slip rates from Model A. The results support the notion that the shear strength of a fault system affects how the elastic strain energy accumulated near the fault is partitioned between earthquake slip and off-fault deformation. Model A1, which has a higher v_0 in the friction law, shows a similar long-term slip rate to that of Model A. Model A5, which has a higher viscosity (implying less off-fault deformation and relaxation) records larger slip rates relative to Model A.

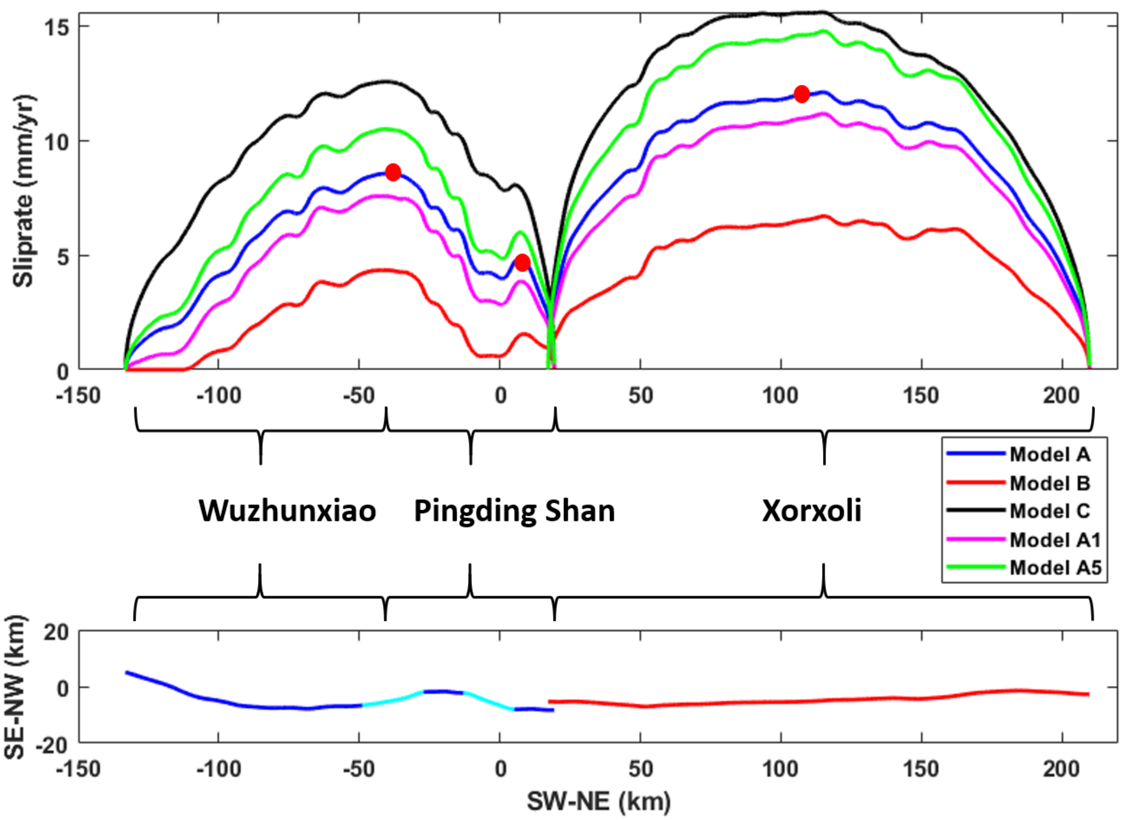

Figure 2. (Top) Long-term slip rates in Model A, B, C, A1 and A5, respectively. In Model A, the maximum long-term slip rate at the Wuzhunxiao, Pingding Shan and Xorxoli segments are about 8.5, 5 and 12 mm/yr, respectively, which are indicated by red dots. The slip rates agree with geodetic and geologic estimates of the long-term slip rate of the ATF. Model B has a high static friction of 0.7. Model C has a low static friction of 0.3. Model A1 has a higher v_0 in the friction law. Model A5 has a higher viscosity. (Bottom) Fault geometry for reference. The blue and red segments indicate the Wuzhunxiao and Xorxoli segments, respectively. The Pingding Shan segment consists of the regional releasing and restraining bends (light blue color).

Model A best fits the paleoseismic and geologic observations along the ATF in this region, including the recurrence interval of 624±411 years and COV of 0.66 determined at the Copper Mine paleoseismic trench site (Yuan et al., 2018), the long-term average ATF slip rate of 9~14 mm /yr (e.g., Shen et al., 2001; Cowgill et al., 2009) for the central ATF, a recent revised long-term slip rate of 4.7 ±0.8 mm/yr east of the Pingding Shan restraining bend at ~ 90.5°E (Prush et al., personal communications), and the slip-per-event about 3-8 meters (Washburn et al., 2001; Elliott et al., 2015). Figure 3a shows modeled recurrence intervals from the earthquake sequence of Model A that closely approximate the recurrence interval and COV reported at the Copper Mine site (Figure 3b). An earthquake event is identified when its slip at the Copper Mine site exceeds 0.2 m. We choose 0.2 m as the threshold because this slip amount is recognizable at paleoseismic sites but is not too large to bar small events from the model. There are 61 such events over the 2500 earthquake cycles simulated. The mean and the standard deviation of the recurrence intervals are 535 and 362 years in Model A, respectively, yielding a COV of 0.68.

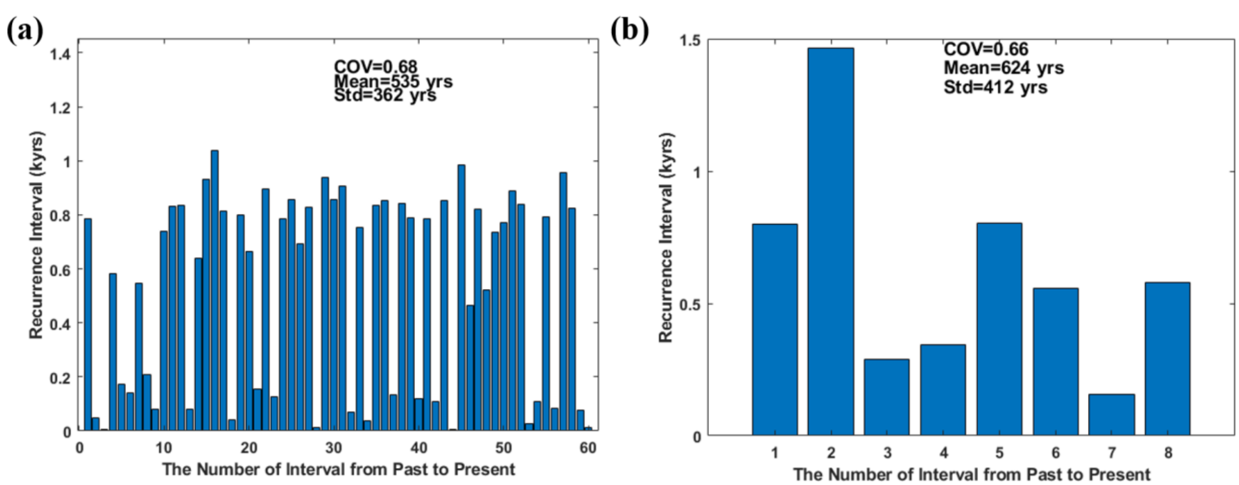

Figure 3. (a) Recurrence intervals from the earthquake sequence of Model A that has a footprint at the Copper Mine site. An earthquake event is defined when its slip exceeds 0.2 m at the Copper Mine site location. The mean and standard deviation of the recurrence interval are 535 and 362 years, respectively. The COV is 0.68. (b) Recurrence intervals from the paleoseismic record at the Copper Mine site on the Xorxoli segment of the central Altyn Tagh fault (Yuan et al., 2018). The record covers a time span of 6000 years and shows 9 earthquake events. The recurrence interval and standard deviation are 624 and 412 years, respectively. The COV is 0.66. Model A reproduces the large variance of recurrence intervals revealed by the paleoseismic record, which ranges from ~100-1000 yr.

The magnitudes of earthquakes shown in Figure 3a ranges from M_w 5.8 to M_w 8.0, assuming slip is uniform to a seismogenic depth of 17 km as suggested by Bouchon and Vallee (2003) for the nearby 2001 Kunlunshan earthquake. However, Jolivet et al. (2008) suggest an 8-10 km locking depth for the ATF, which would yield magnitudes from M_w 5.6 to M_w 7.9. The maximum slip for these events ranges from 0.39 to 12.66 m, with a mean of 6.70 m and a standard deviation of 4.69 m. The mean agrees with the slip amount per event of 3-8 m inferred from geologic data (Washburn et al., 2001; Washburn et al., 2003; Elliott et al., 2015).

4.2 Dynamic rupture models from best-fit simulation parameters

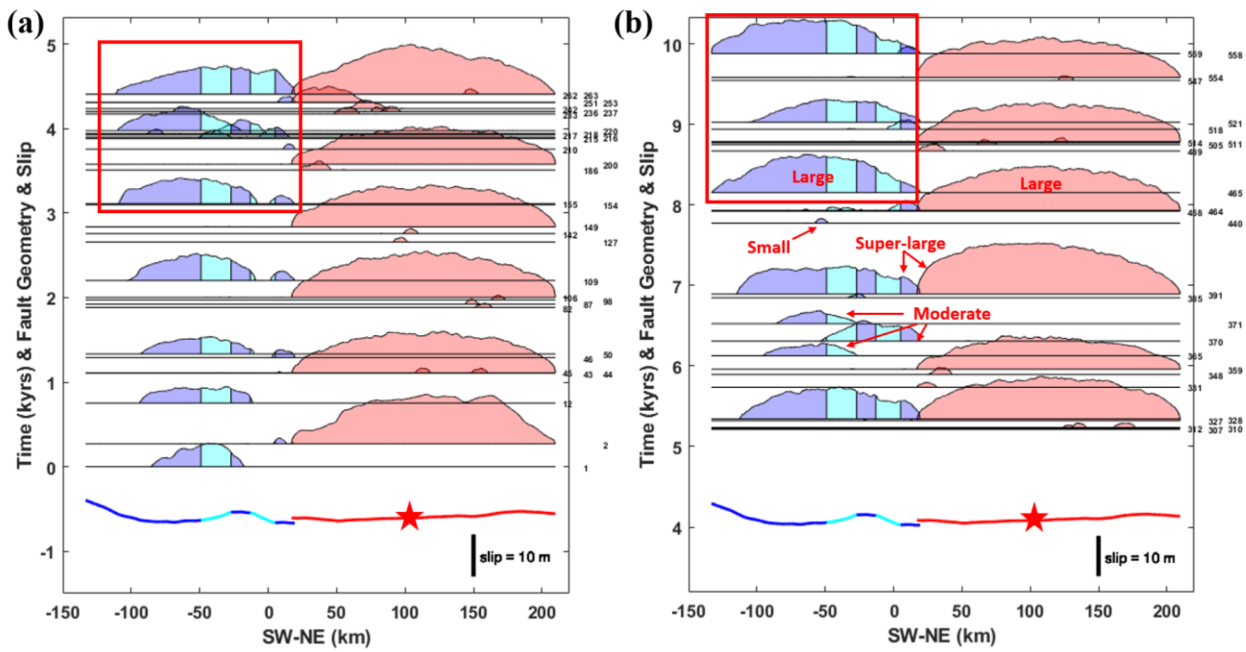

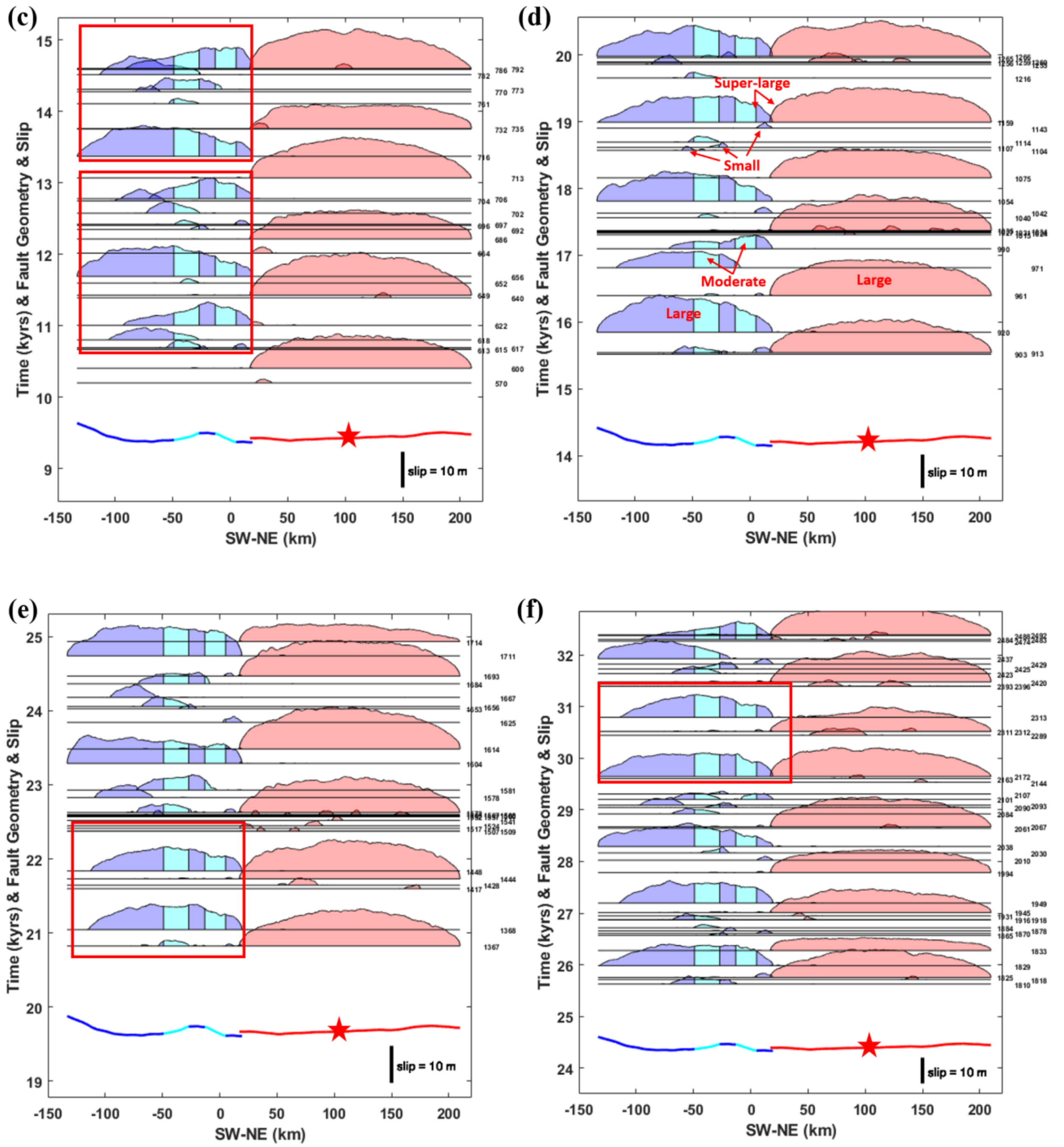

Figure 4. Slip distributions of earthquake events (maximum slip > 1 m) in Model A during the 32.5 kyrs simulated. Panels a-e shows slip distributions every 5 kyrs and panel f shows slip distributions in the last 7.5 kyrs. The fault geometry is shown at the bottom of each panel. A bar of 10 m slip is given for reference in each panel. Event numbers are shown on the right edge of each panel. The paleoseismic site Copper Mine is denoted as a star on the fault geometry. Examples of small, moderate, large, and super-large ruptures are indicated in panels b and d (see Section 4.2 for details of these definitions). Red rectangles in panels a and c outline rupture patterns that involve a mixture of small, moderate, and large events. Red rectangles in panels b, e and f show rupture patterns that involve mainly ruptures combining the Wuzhunxiao and Pingding Shan segments. The blue and red segments indicate the Wuzhunxiao and Xorxoli segments, respectively. The Pingding Shan segment consists of

the regional releasing and restraining bends (light blue color).

Figure 4 show slip distributions of earthquake events with maximum slip over 1 m from Model A. Here, we qualitatively define four types of ruptures in the earthquake sequence of Model A. Small events have rupture extents less than 20 km ($M_w < 7.1$ assuming the locking depth of 17 km). Moderate events rupture tens of kilometers with an upper length limit of 100 km (M_w = 7.1 - 7.6). Large ruptures exceed 100 km ($M_w > 7.6$) which typically involve the whole Xorxoli segment or the combined Wuzhunxiao and Pingding Shan segments. Super-large ruptures span the entire modeled fault system. Examples of small to super-large events are labelled in Figure 4b and 4d, respectively. The Wuzhunxiao and Pingding Shan segments show two primary rupture patterns. One pattern involves a mixture of small, moderate, and large events, as indicated by red rectangles in Figure 4a and 4c. The other pattern consists of mainly large events that span the combined length of the Wuzhunxiao and Pingding Shan segments, as outlined by red rectangles in Figure 4b, 4e, and 4f. The prominent restraining and releasing bends contribute to the complex patterns because ruptures frequently terminate at their ends. About every 1-2 kyrs a large rupture occurs that spans both bends but is frequently stopped by the releasing step-over between the Pingding Shan and Xorxoli segments. In contrast, the Xorxoli segment is relatively straight and shows less macroscopic geometric complexity. As a result, the rupture pattern is dominated by relatively periodic large ruptures and irregularly recurring small and moderate events. We note that if the Xorxoli segment were perfectly straight and the loading was constant over time, we would expect more periodic ruptures of the whole Xorxoli segment, which cannot explain the 0.66 COV determined by paleoseismology. Local fault geometric complexities and the irregularly recurring small and moderate events therefore contribute to the high COV on the relatively straight Xorxoli segment.

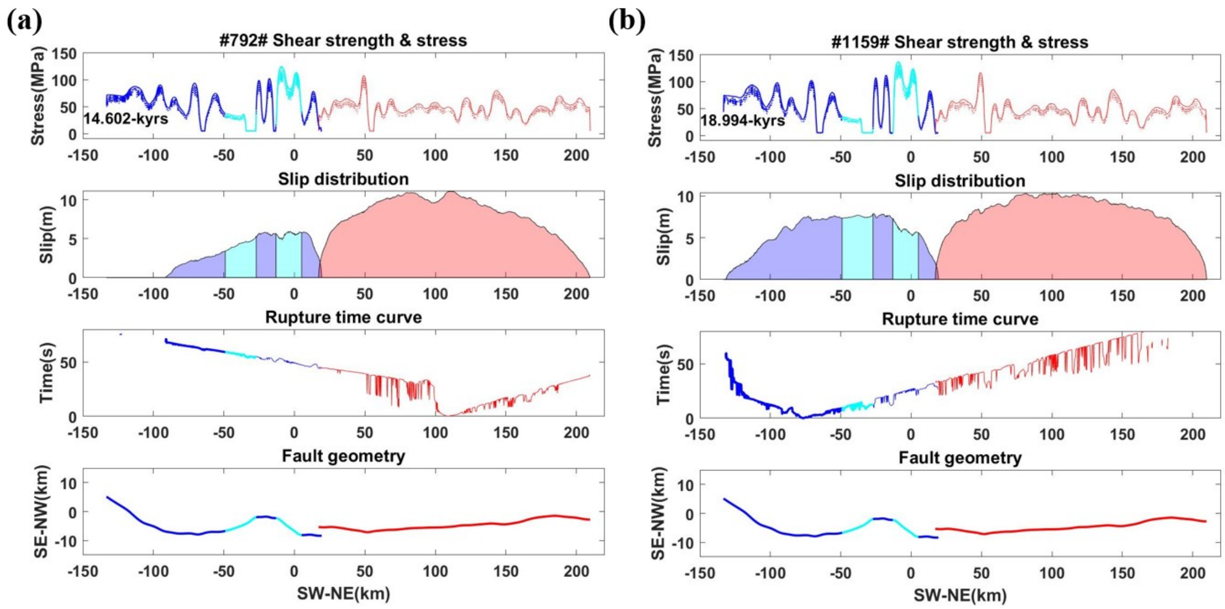

Figure 5. Details of dynamic ruptures of super-large events #792 (a) and #1159 (b), respectively. The rupture details (top to bottom of the figure) include shear stress and strength distributions before ruptures, final slip distributions, rupture time curves, and the fault geometry for reference.

Super-large earthquakes that rupture all three complexities within the earthquake gate are possible but rare. In the 2500 earthquake cycles simulated in Model A, seven events span the entire fault. Six of these events nucleate on the Xorxoli segment, indicating it is a favorable segment for nucleation of super-large ruptures. The seventh initiates on the Wuzhunxiao segment. The super-large ruptures exhibit two types of dynamics. Figure 5a and 5b show details of rupture dynamics for two super-large ruptures, including the stress conditions before rupture, coseismic slip distributions, and rupture time curves. (Rupture details of the other 5 super-large events are provided in Figure S1-S5 in the supplementary material.) They show somewhat different dynamics, indicating the complexity of dynamic ruptures in a geometrically realistic fault system. The first type represents six super-large ruptures that nucleate on the Xorxoli segment and propagate westward through the Pingding Shan earthquake gate. The difference among them is the nucleation location along the Xorxoli segment as shown by rupture details of those events in the supplementary material. Figure 5b shows the event that nucleates on the Wuzhunxiao segment. Figure S6 includes nucleation locations of all the events presented in Figure 4. Figure S6 demonstrates that earthquakes tend to nucleate where the fault is about parallel to the general ATF strike and near bends or the step-over. In addition, many earthquakes nucleate on the regional releasing bend but nucleation on the regional restraining bend is rare.

The releasing stepover is more effective as a barrier to dynamically propagating ruptures than the restraining bend in our models. For example, ruptures propagating from the Wuzhunxiao segment can break the Pingding Shan restraining bend, but are often stopped by the stepover. The combination of the two fault complexities leads to a low occurrence rate of super-large ruptures. There are 193 earthquake events shown in Figure 4 with magnitudes ranging from M_w 6.22 to M_w 8.0 (assuming a locking depth of 17 km). Given seven super-large ruptures over the 32.5 kyr simulated, the earthquake sequence yields a low occurrence rate of super-large ruptures at 3.6% for earthquakes over M_w 6.22 and an average recurrence interval of about 4.6 kyrs.

4.3 On-fault stress states preceding super-large ruptures

Figure 6a shows shear strength distributions before super-large events #263, #391, #792, #1159, #1266 and #2172 from Model A, respectively. Figure 6c shows fault strikes variations along the fault. Wide ranges of positive and negative numbers indicate regional restraining and releasing bends over tens of kilometers, which are colored in light blue. In addition, these regional bends contain local restraining bends and releasing bends at finer spatial scales in a few kilometers, as indicated by vertical dashed lines where strikes change sharply over short distances. Figure 6d shows the fault geometry. The shear strengths before super-large ruptures are very heterogeneous. The heterogeneity is strongly correlated with fault geometry, with generally high strengths at the regional restraining bend and low strengths at the regional releasing bend. For example, the prominent Pingding Shan restraining bend shows an overall shear strength well over 120 MPa, while the releasing bend west to the Pingding Shan has strength below 40 MPa, with some locations reaching the minimum 5 MPa permitted by the model (calculated by multiplying the minimum absolute normal stress 10 MPa by the static friction coefficient 0.5). On the other hand, the local strength peaks and troughs are correlated with local restraining and releasing bends. For example, within the Pingding Shan restraining bend, a strength trough corresponds to the local releasing bend (indicated by the dash red vertical line).

Second, the shear strength of the fault system evolves to become more heterogenous as more ruptures occur, as shown in Figure 6b. We calculate ratios of shear strength of super-large events #391, #792, #1159, #1266 and #2172 relative to the shear strength of event #263, the first super-large rupture in the earthquake sequence, at every fault node. Figure 6b shows the distribution of these ratios. A ratio of 1 at a fault node indicates the shear strength does not deviate from that in event #263. The accumulation of stress heterogeneity is indicated by an increase in the ratio of shear strength at restraining bends and a decrease at releasing bends. The on-fault stress conditions deviate substantially from the distribution calculated by simply resolving a uniform regional stress field onto the fault based on fault geometry.

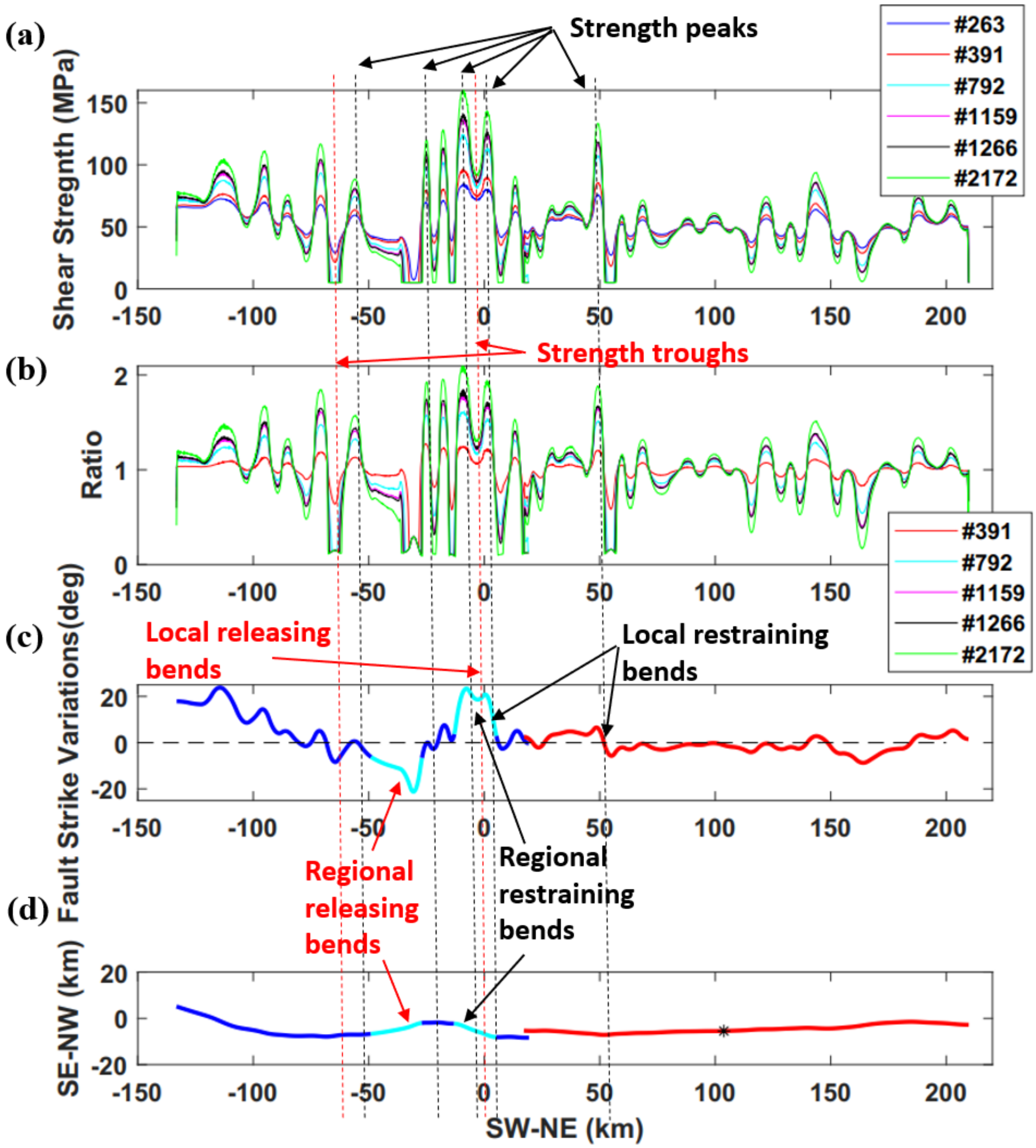

Figure 6. (a) Shear strength distributions before super-large events. Event numbers are shown in the legend. (b) Distributions of shear strength ratios for events #391, #792, #1159, #1266 and #2172 relative to the shear strength of event #263, respectively. (c) Fault strike variations along the fault. Zero values, the dashed horizontal line, indicates that the fault is parallel to the general strike of ATF. Wide ranges of positive and negative angles, that are colored in light blue, stand for the regional restraining and releasing bends, respectively. These regional bends contain local restraining and releasing bends at finer spatial scales, which are indicated by sharp changes of strike angles over short distances. In general, the regional restraining and releasing bends correspond to high and low shear strengths in panel a. The local stress peaks and troughs are also correlated with local restraining and releasing bends, as indicated by the vertical black and red dash lines. (d) Reference fault geometry. The Copper Mine paleoseismic site is denoted by the star.

4.4 Mechanical effects of the key parameters

4.4.1 Static friction

Static friction affects the long-term slip rate distribution by determining the amount of elastic strain partitioned between earthquake slip and off-fault deformation. Model B and Model C have a static friction of 0.7 and 0.3, representing strong and weak end-member fault systems, respectively. As shown in Figure 2, Model B yields long-term slip rates slightly less than half of those determined in Model A, while Model C yields a much higher long-term slip rate with peaks over 15 mm/yr. Low static friction reduces the degree of strength heterogeneity caused by fault geometry during both long-term loading and dynamic ruptures. For an on-fault normal stress ranges from 100 MPa to 200 MPa with static friction of 0.3, the shear strength would vary from 30 MPa to 60 MPa. For the same fault system with a static friction of 0.7, the shear strength would vary from 70 MPa to 140 MPa instead. A fault system with low static friction therefore tends to reduce stress heterogeneity associated with the fault geometry.

Figure 7 shows slip distributions of dynamic ruptures in Model B (Figure 7a) and Model C (Figure 7b), respectively. The slip patterns are characteristic in each model for the time ranges chosen. The strong fault of Model B shows fragmented rupture patterns that include small, moderate, and large earthquakes, while the weak fault of Model C is mainly dominated by large and occasionally super-large earthquakes. The rupture pattern of Model B is similar to that of Model A. Figure 8 shows recurrence intervals and their statistics at the Copper Mine site from Model B (Figure 8a) and Model C (Figure 8b), respectively. Their COVs are 0.70 and 0.54, and their mean recurrence intervals are 896 years and 462 years, respectively. Model B is more in line with Model A in terms of COV, while Model C yields shorter recurrence intervals and a smaller COV compared to Model A.

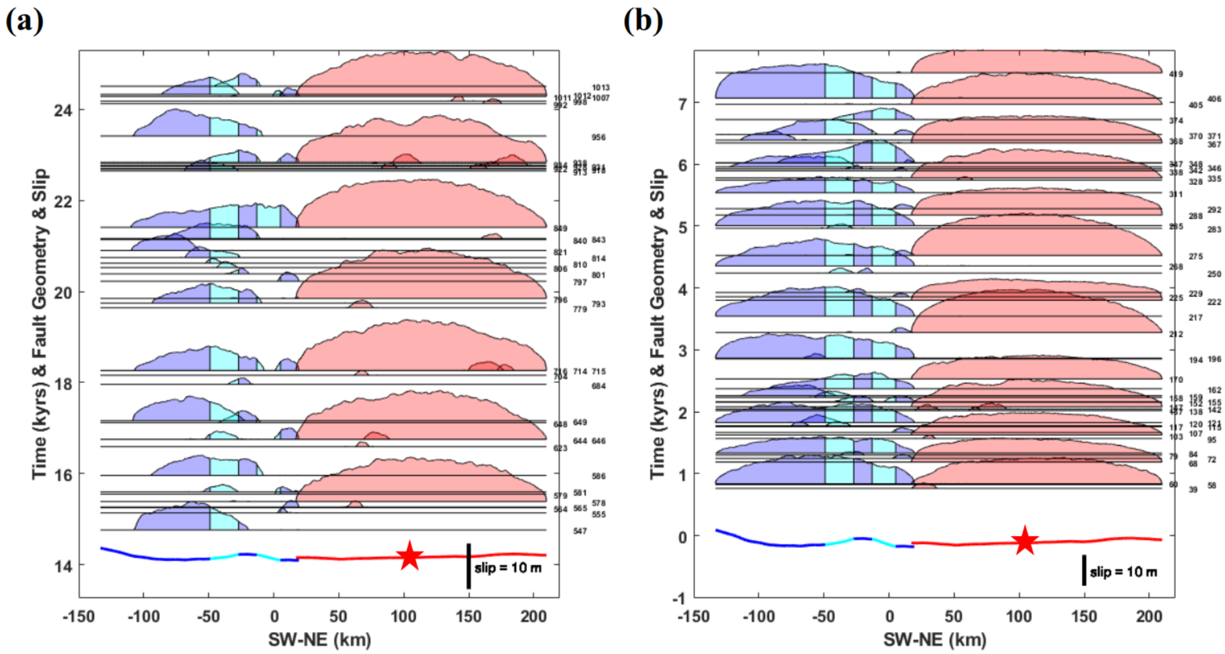

Figure 7. (a) Slip distributions of earthquake events (maximum slip > 1 m) in the high friction model (Model B), 15 to 25 kiloyears after the start of the simulation. (b) Slip distributions of earthquake events in the low friction model (Model C) in the first 7.5 kyrs after model initiation. The fault geometry is shown at the bottom of each panel. A bar of 10 m slip is given for reference. Event numbers are shown on the right edge of each panel. The regional restraining and releasing bends are colored in light blue. The Copper Mine paleoseismic trench is denoted as a star on the fault geometry.

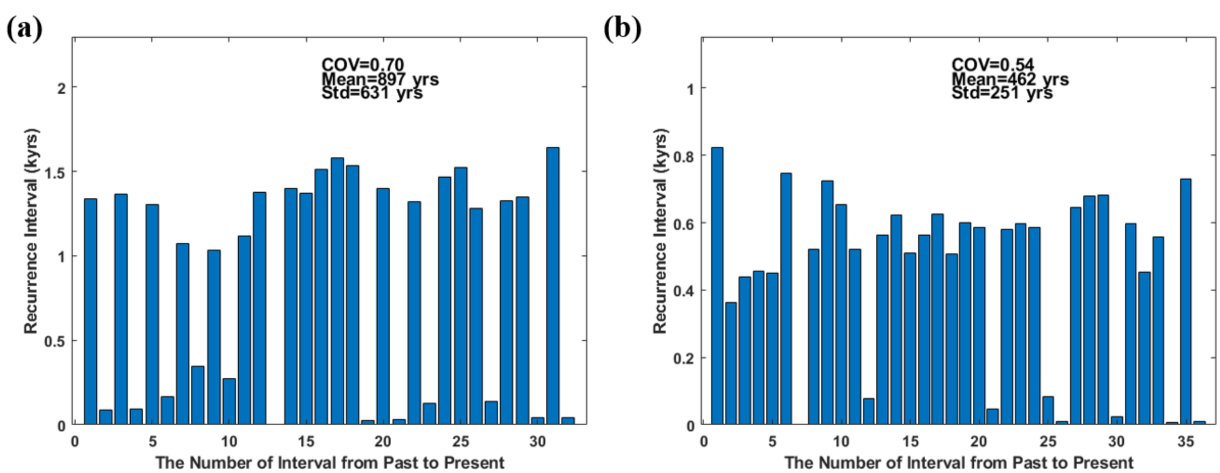

Figure 8. (a) Recurrence intervals at the Copper Mine site from the earthquake sequence of Model B. An earthquake is defined when its slip at the Copper Mine site exceeds 0.2 m. The mean and standard deviation of the recurrence interval are 896 and 631 years, respectively. The COV is 0.70. (b) Recurrence intervals at the Copper Mine site from the earthquake sequence of Model C. The mean and standard deviation of the recurrence interval are 462 and 251 years, respectively. The COV is 0.54.

4.4.2 The effect of apparent stress drop

Table 2 summarizes the statistics of recurrence intervals and slips at the Copper Mine paleoseismic trench site from Model A and Models A1-A5. The means and standard deviations of recurrence intervals and slips from various models are visualized in Figure 9a and 9b, respectively. Here we compare the results from Model A1 and Model A to examine the effect of apparent stress drop. Compared with Model A, the only change in Model A1 is an increase in the dynamic friction coefficient (f_d), from 0.43 in Model A to 0.45 in Model A1 (Table 1). Given $f_s = 0.5$ and $\sigma_a = 100$ MPa, this change results in a smaller apparent stress drop of 5 MPa in Model A1, compared with 7 MPa in Model A. The reduction of the apparent stress drop increases the COV of Model A1 to 0.81 from 0.68 in Model A (Table 2). The recurrence interval and slip are comparable with those in Model A, with smaller mean values in Model A1. The difference in maximum long-term slip rate on the Wuzhunxiao and Xorxoli segments is only ~1 mm/yr (Figure 2), implying a minor effect of apparent stress drop on the long-term slip rate.

Table 2. Summary of earthquake rupture parameters at the Copper Mine site obtained from the multicycle dynamic models.

Model name	Mean of recurrence interval, years	Std of recurrence interval, years	COV	Mean of peak slip, m	Std of peak slip, m	Number of events with peak slips over 1 m/ total cycles modeled
A	535	362	0.68	6.70	4.69	61/2500
A1	425	344	0.81	5.27	3.98	33/1500
A2	1031	350	0.34	12.04	4.01	27/1500
A3	523	248	0.47	6.72	3.29	61/1500
A4	397	372	0.94	5.34	6.00	30/1500
A5	502	281	0.56	7.67	4.46	36/1500

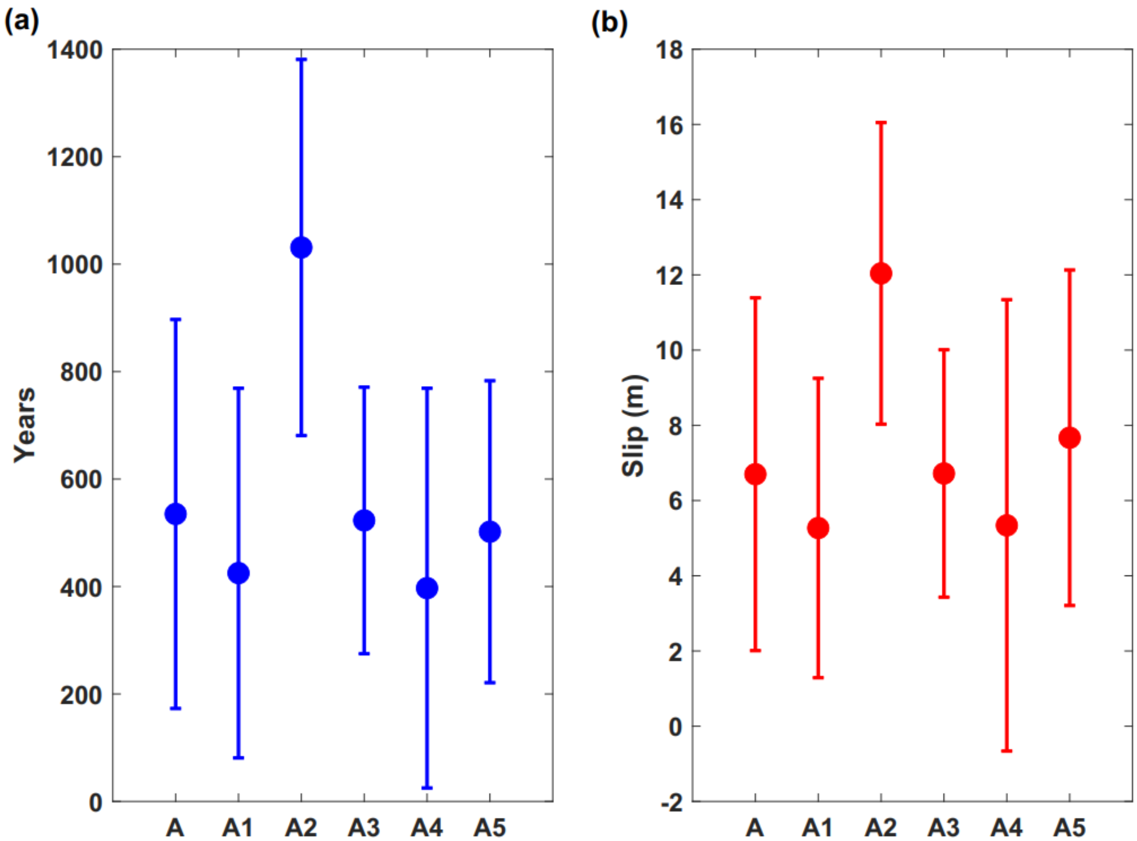

Figure 9. (a) Means and standard deviations of recurrence intervals at the Copper Mine site from Models A, A1-A5, respectively. (b) Means and standard deviations of slips at the Copper Mine site from Models A, A1-A5, respectively.

4.4.3 The effect of rate and slip dependence of friction

We explore the effect of rate dependence of friction in dynamic ruptures on the statistics of the fault system by adjusting the restrengthening friction (f_r) and the threshold slip velocity (v_0). In Model A2, f_r is lower than that in Model A (Table 1). In Model A3, the threshold slip velocity v_0 is larger than that in Model A (Table 1). As shown in Duan (2019), a lower f_r or a larger v_0 favors a more gradual friction restrengthening process during dynamic ruptures. We obtain lower COVs of 0.34 and 0.47 in Models A2 and A3, respectively, compared with that in Model A. It suggests that more gradual friction restrengthening in dynamic ruptures favors more periodicity of recurrence intervals.

Model A4 has a larger d_0 than Model A (Table 1), which indicates a larger fracture energy and less rapid energy release during dynamic ruptures. An increase in d_0 results in an increase in the number of small events, leading to an increase in rupture pattern heterogeneity (indicated by a higher COV of 0.94, Table 2). These results indicate that a fault system with a realistic fault geometry and dynamic ruptures with a slower energy release rate and more rapid restrengthening will yield a larger COV.

4.4.4 The effect of viscosity.

The viscosity in our models affects the partitioning of the elastic strain energy between earthquake rupture and off-fault deformation. Higher viscosities tend to yield higher long-term slip rates (Duan et al., 2019). Model A5, which has a higher viscosity of 3.5×10^{22} Pa s than Model A (Table 1), yields larger long-term slip rates compared to that of Model A (Figure 2), agreeing with the previous study.

5. Discussion

We find that multicycle dynamic rupture models with realistic fault geometry can reproduce the mean and COV of recurrence intervals documented at the Copper Mine paleoseismic trench site on the Xorxoli segment over the past 6000 years. Two questions emerge: why does fault geometry matter, and how does it affect stress state? Dieterich and Smith (2010) show that stress heterogeneity from geometric interactions at irregularities along nonplanar faults causes the slip solutions to diverge from those of planar faults and leads to nonlinear scaling of fault slip with rupture dimension in a purely elastic medium. The divergence increases with the fractal features of the fault geometry and the stress heterogeneity may progressively impede slip. Dieterich and Richards-Dinger (2010) uses an efficient, quasi-static fault system earthquake simulator, RSQSim, to simulate earthquake catalogs with up to 10^6 events with magnitudes from ~M_w 4.5 to M_w 8. They demonstrate that fault system geometry is the major driver to establish the characteristics of stresses that control earthquake recurrence statistics. Dynamic ruptures on rough fault geometry also yield heterogeneous stresses and slips and excite waves over a wide range of frequency that is important for ground motion applications (Dunham et al., 2011b; Shi and Day, 2013). Combining both the long-term earthquake cycles and dynamic ruptures, our multicycle dynamic models demonstrate that stress heterogeneity associated with fault geometric complexities is impacted by a feedback loop of three processes over multiple earthquake cycles. First, dynamic ruptures passing fault bends or stepovers will induce heterogenous stresses. Second, during the interseismic periods, tectonic loading and stress relaxation will lead to fault-strike dependent stress accumulation and relaxation. Third, the stress history from past earthquakes will serve as the initial conditions for the next earthquake cycle. Therefore, as illustrated in Figure 6, heterogeneous stresses preceding dynamic ruptures evolve over earthquake cycles and are closely correlated with fault geometry.

The overall shear strength of the fault system, parameterized by the static friction level (f_s) in our models, affects both the long-term slip rate of the system and the details of rupture dynamics. A moderate value of f_s=0.5 (Model A) best fits geologic and paleoseismic observations. We also examine two end members of static friction levels at 0.7 (Model B) and 0.3 (Model C) representing a very strong and a very weak fault system, respectively. The weak fault, Model C, tends to yield large earthquakes because the low static friction smooths the fault geometry-related stress heterogeneities, favoring unimpeded ruptures. Based on empirical relations from fault mapping of past earthquakes (Biasi and Wesnousky, 2017), the Pingding Shan restraining bend should be a strong barrier to ruptures. But in the case of Model C, it barely stops dynamically propagating ruptures. The strong fault model (Model B) shows a more fragmented rupture pattern than Model A.

The initial stress condition, which is a key ingredient in dynamic rupture models, is poorly constrained. As shown in Figure 6, on-fault stresses become rather heterogeneous after many earthquake cycles on the fault system with realistic geometry. Our results imply that, to prescribe a heterogeneous initial stress field for single-event dynamic rupture models, stresses resolved from a regional stress field based on fault geometry should be increased/decreased at regional and local restraining/releasing bends where substantial strike changes occur to take into account stress heterogeneity inherited from past earthquakes.

There are still disparities between paleoseismic records and the best fit Model A in terms of recurrence intervals and the COV. Two possibilities may explain the disparity. First, the limited sample size of paleoseismic records, subject to uncertainties in dating, affects the mean and COV of recurrence intervals. Second, the realistic fault geometry in the multicycle dynamic rupture models alone may not account for all the heterogeneities in earthquake processes. Given the uncertainties in paleoseismic datasets, we aim to capture only the major features, rather than fine-tuning our models for a perfect fit. The key message from the models is that a realistic fault geometry can account for much of the complexity in earthquake recurrence intervals revealed by the paleoseismic record.

6. Conclusion

In this study we simulate multicycle dynamic ruptures of the Pingding Shan earthquake gate along the Altyn Tagh Fault in northwest China. We adopt a 350 km-long fault geometry and run 2500 earthquake cycles in our best fit model. The mean and COV of recurrence intervals from the model at the Copper Mine site of 535 years and 0.68, respectively, compare favorably with the 624 years and 0.66 obtained from the paleoseismic record at the site on the Xorxoli segment. The maximum long-term slip rates on the Wuzhunxiao and Xorxoli segment of about 8.5 and 12 mm/yr, respectively, match estimates of geodetically and geologically determined slip rates along the ATF of 9~14 mm/yr. In addition, our model yields a slip rate of about 5 mm/yr east of the Pingding restraining bend, agreeing with a recent geologic estimate of 4.7±0.8 mm/yr (Prush et al., personal communications) and suggesting a reduction of slip affected by the restraining bend and fault tips. The average slip-per-event from the model is 6.7±4.69 m for earthquakes that break the Copper Mine site, in agreement with the slip-per-event estimates from geomorphic offset measurements of 3-8 m in the region (Washburn et al., 2001; Elliott, 2014).

The earthquake sequences on the fault system from the best-fit model show complex rupture patterns. The Wuzhunxiao and Pingding Shan segments show a mixture of small and moderate earthquakes that are segmented by the regional releasing and restraining bends and large earthquakes that break the combined Wuzhunxiao and Pingding Shan segments. The Xorxoli segment, which lacks major geometric complexities, tends to serve as the nucleation location of super-large earthquakes that rupture the span of the model. Both the Pingding Shan restraining bend and the releasing stepover impede dynamically propagating ruptures. The Pingding Shan step-over is more effective as a barrier to ruptures in the simulations, but the combination of the two makes the Pingding Shan earthquake gate an effective barrier to super-large, system-spanning ruptures. Super-large ruptures have a recurrence interval of ~4.6 kyrs and a rate of 3.6% for earthquakes over M_w 6.22 in the fault system. The Aksay bend that is east of the Pingding Shan gate is an effective barrier to dynamically propagating ruptures and passes only about 10% of ruptures. If we assume that the Pingding Shan earthquake gate is independent of the Aksay bend, we could estimate that even larger earthquakes are vanishingly rare.

The overall static friction level of the fault system, i.e., fault strength, affects strain partitioning between on-fault slip and off-fault deformation and, consequently, the long-term slip rate of the fault system. It also affects rupture dynamics. Lower static friction, i.e., a weak fault, tends to reduce the effectiveness of the restraining bend as a rupture barrier and increases the proportion of energy partitioned to on-fault earthquake slip. The weak fault favors large ruptures and occasional super-large ruptures.

Our models illustrate the critical role of realistic fault geometries to the dynamics of a fault system. The feedback loop of stress heterogeneity inherited from past earthquakes, dynamic ruptures, and interseismic deformation, leads to fault-geometry-related stress heterogeneity. Complex rupture patterns arise from the heterogenous stress condition, which evolves continuously over earthquake cycles. In addition, rapid and strong restrengthening during dynamic rupture is necessary to explain the 0.66 COV of recurrence intervals at the Copper Mine paleoseismic trench site, especially on the relatively straight Xorxoli segment, which tends to favor unimpeded rupture propagation. Our models indicate that the on-fault stress conditions before earthquakes are much more heterogeneous than the stresses calculated by simply resolving a uniform stress field onto a geometrically complex fault based solely on local fault geometry. The fault-geometry-related stress heterogeneity presented in this study may provide a guidance to set up initial stresses for single-event dynamic rupture simulations that accounts for the effect of past earthquakes.

Acknowledgement: We thank Editor Ling Chen, Julian Lozos and an anonymous reviewer for their constructive reviews that improve the manuscript. The work is funded by National Science Foundation (NSF) Awards EAR-1524743, EAR-1524734 and EAR-2013695. The work is also supported by the National Natural Science Foundation of China (NSFC) (U1839203). Figure 1 is generated by GMT 5.1. Other figures are generated by MATLAB (R2017a). We thank Texas A&M High Performance Research Computing (http://hprc.tamu.edu/) for providing the advanced computing resources used in the study.

References

Aagaard, B.T., Heaton, T.H., Hall, J.F., 2001. Dynamic earthquake ruptures in the presence of lithostatic normal stresses: Implications for friction models and heat production. Bull. Seismol. Soc. Am. 91, 1765-1796

Andrews, D.J., 1976. Rupture Velocity of Plane Strain Shear Cracks. J. Geophys. Res. 81, 5679-5687

Bendick, R., Bilham, R., Freymueller, J., Larson, K., Yin, G., 2000. Geodetic evidence for a low slip rate in the Altyn Tagh fault system. Nature 404, 69-72

Biasi, G.P., Wesnousky, S.G., 2016. Steps and Gaps in Ground Ruptures: Empirical Bounds on Rupture Propagation. Bull. Seismol. Soc. Am. 106, 1110-1124

Biasi, G.P., Wesnousky, S.G., 2017. Bends and Ends of Surface Ruptures. Bull. Seismol. Soc. Am. 107, 2543-2560

Bouchon, M., Vallee, M., 2003. Observation of long supershear rupture during the magnitude 8.1 Kunlunshan earthquake. Science 301, 824-826

Byerlee, J., 1978. Friction of Rocks. Pure Appl. Geophys. 116, 615-626

Cohee, B.P., Beroza, G.C., 1994. Slip distribution of the 1992 Landers earthquake and its implications for earthquake source mechanics. Bull. Seismol. Soc. Am. 84, 692-712

Cowgill, E., 2007. Impact of riser reconstructions on estimation of secular variation in rates of strike–slip faulting: Revisiting the Cherchen River site along the Altyn Tagh Fault, NW China. Earth Planet. Sci. Lett. 254, 239-255

Cowgill, E., Gold, R.D., Xuanhua, C., Xiao-Feng, W., Arrowsmith, J.R., Southon, J., 2009. Low Quaternary slip rate reconciles geodetic and geologic rates along the Altyn Tagh fault, northwestern Tibet. Geology 37, 647-650

Cowgill, E., Yin, A., Arrowsmith, J.R., Feng, W.X., Shuanhong, Z., 2004. The Akato Tagh bend along the Altyn Tagh fault, northwest Tibet 1: Smoothing by vertical-axis rotation and the effect of topographic stresses on bend-flanking faults. Geol. Soc. Am. Bull. 116, 1423-1442

Day, S.M., 1982. Three-dimensional simulation of spontaneous rupture: the effect of nonuniform prestress. Bull. Seismol. Soc. Am. 72, 1881-1902

Di Toro, G., Goldsby, D.L., Tullis, T.E., 2004. Friction falls towards zero in quartz rock as slip velocity approaches seismic rates. Nature 427, 436-439

Dieterich, J.H., 1979. Modeling of Rock Friction .1. Experimental Results and Constitutive Equations. J. Geophys. Res. 84, 2161-2168

Dieterich, J.H., Richards-Dinger, K.B., 2010. Earthquake Recurrence in Simulated Fault Systems. Pure Appl. Geophys. 167, 1087-1104

Dieterich, J.H., Smith, D.E., 2010. Nonplanar Faults: Mechanics of Slip and Off-fault Damage, in: Ben-Zion, Y., Sammis, C. (Eds.), Mechanics, Structure and Evolution of Fault Zones. Birkhäuser Basel, Basel, pp. 1799-1815.

Duan, B., 2019. Multicycle Dynamics of the Aksay Bend Along the Altyn Tagh Fault in Northwest China: 1. A Simplified Double Bend. Tectonics 38, 1101-1119

Duan, B., Liu, Z., Elliott, A.J., 2019. Multicycle Dynamics of the Aksay Bend Along the Altyn Tagh Fault in Northwest China: 2. The Realistically Complex Fault Geometry. Tectonics 38, 1120-1137

Duan, B., Oglesby, D.D., 2005. Multicycle dynamics of nonplanar strike‐slip faults. Journal of Geophysical Research: Solid Earth (1978–2012) 110

Duan, B., Oglesby, D.D., 2006. Heterogeneous fault stresses from previous earthquakes and the effect on dynamics of parallel strike-slip faults. J Geophys Res-Sol Ea 111

Duan, B., Oglesby, D.D., 2007. Nonuniform prestress from prior earthquakes and the effect on dynamics of branched fault systems. J. Geophys. Res. 112

Dunham, E.M., Belanger, D., Cong, L., Kozdon, J.E., 2011a. Earthquake Ruptures with Strongly Rate-Weakening Friction and Off-Fault Plasticity, Part 1: Planar Faults. Bull. Seismol. Soc. Am. 101, 2296-2307

Dunham, E.M., Belanger, D., Cong, L., Kozdon, J.E., 2011b. Earthquake Ruptures with Strongly Rate-Weakening Friction and Off-Fault Plasticity, Part 2: Nonplanar Faults. Bull. Seismol. Soc. Am. 101, 2308-2322

Elliott, A.J., 2014. Control of Rupture Behavior by a Restraining Double-bend from Slip Rates on the Altyn Tagh Fault. Ph.D. Dissertation. University of California, Davis.

Elliott, A.J., Dolan, J.F., Oglesby, D.D., 2009. Evidence from coseismic slip gradients for dynamic control on rupture propagation and arrest through stepovers. J Geophys Res-Sol Ea 114

Elliott, A.J., Oskin, M.E., Liu-Zeng, J., Shao, Y., 2015. Rupture termination at restraining bends: The last great earthquake on the Altyn Tagh Fault. Geophys. Res. Lett. 42, 2164-2170

Elliott, J.R., Biggs, J., Parsons, B., Wright, T.J., 2008. InSAR slip rate determination on the Altyn Tagh Fault, northern Tibet, in the presence of topographically correlated atmospheric delays. Geophys. Res. Lett. 35

Gold, R.D., Cowgill, E., Arrowsmith, J.R., Gosse, J., Chen, X., Wang, X.-F., 2009. Riser diachroneity, lateral erosion, and uncertainty in rates of strike-slip faulting: A case study from Tuzidun along the Altyn Tagh Fault, NW China. J Geophys Res-Sol Ea 114

Hamling, I.J., Hreinsdottir, S., Clark, K., Elliott, J., Liang, C., Fielding, E., Litchfield, N., Villamor, P., Wallace, L., Wright, T.J., D'Anastasio, E., Bannister, S., Burbidge, D., Denys, P., Gentle, P., Howarth, J., Mueller, C., Palmer, N., Pearson, C., Power, W., Barnes, P., Barrell, D.J., Van Dissen, R., Langridge, R., Little, T., Nicol, A., Pettinga, J., Rowland, J., Stirling, M., 2017. Complex multifault rupture during the 2016 Mw 7.8 Kaikoura earthquake, New Zealand. Science 356, eaam7194

Harris, R.A., Barall, M., Aagaard, B., Ma, S., Roten, D., Olsen, K., Duan, B., Liu, D., Luo, B., Bai, K., Ampuero, J.P., Kaneko, Y., Gabriel, A.A., Duru, K., Ulrich, T., Wollherr, S., Shi, Z., Dunham, E., Bydlon, S., Zhang, Z., Chen, X., Somala, S.N., Pelties, C., Tago, J., Cruz–Atienza, V.M., Kozdon, J., Daub, E., Aslam, K., Kase, Y., Withers, K., Dalguer, L., 2018. A Suite of Exercises for Verifying Dynamic Earthquake Rupture Codes. Seismol. Res. Lett. 89, 1146-1162

Harris, R.A., Barall, M., Archuleta, R., Dunham, E., Aagaard, B., Ampuero, J.P., Bhat, H., Cruz-Atienza, V., Dalguer, L., Dawson, P., Day, S., Duan, B., Ely, G., Kaneko, Y., Kase, Y., Lapusta, N., Liu, Y., Ma, S., Oglesby, D., Olsen, K., Pitarka, A., Song, S., Templeton, E., 2009. The SCEC/USGS Dynamic Earthquake Rupture Code Verification Exercise. Seismol. Res. Lett. 80, 119-126

Harris, R.A., Day, S.M., 1993. Dynamics of fault interaction: parallel strike-slip faults. J. Geophys. Res. 98, 4461

Heaton, T.H., 1990. Evidence for and Implications of Self-Healing Pulses of Slip in Earthquake Rupture. Phys. Earth Planet. Inter. 64, 1-20

Jaeger, J.C., 1969. Behaviour of Actual Materials, Elasticity, Fracture and Flow: with Engineering and Geological Applications. Springer Netherlands, Dordrecht, pp. 49-106.

Jolivet, R., Cattin, R., Chamot-Rooke, N., Lasserre, C., Peltzer, G., 2008. Thin-plate modeling of interseismic deformation and asymmetry across the Altyn Tagh fault zone. Geophys. Res. Lett. 35

Kaiser, A., Balfour, N., Fry, B., Holden, C., Litchfield, N., Gerstenberger, M., D'Anastasio, E., Horspool, N., McVerry, G., Ristau, J., Bannister, S., Christophersen, A., Clark, K., Power, W., Rhoades, D., Massey, C., Hamling, I., Wallace, L., Mountjoy, J., Kaneko, Y., Benites, R., Van Houtte, C., Dellow, S., Wotherspoon, L., Elwood, K., Gledhill, K., 2017. The 2016 Kaikōura, New Zealand, Earthquake: Preliminary Seismological Report. Seismol. Res. Lett. 88, 727-739

King, G., Nabelek, j., 1985. Role of Fault Bends in the Initiation and Termination of Earthquake Rupture. Science 228, 984-987

Liu, D., Duan, B., Luo, B., 2020. EQsimu: a 3-D finite element dynamic earthquake simulator for multicycle dynamics of geometrically complex faults governed by rate- and state-dependent friction. Geophys. J. Int. 220, 598-609

Lozos, J.C., Oglesby, D.D., Duan, B., Wesnousky, S.G., 2011. The Effects of Double Fault Bends on Rupture Propagation: A Geometrical Parameter Study. Bull. Seismol. Soc. Am. 101, 385-398

Luo, B., Duan, B., 2018. Dynamics of Nonplanar Thrust Faults Governed by Various Friction Laws. J Geophys Res-Sol Ea 123, 5147-5168

Madariaga, R., Olsen, K., Archuleta, R., 1998. Modeling dynamic rupture in a 3D earthquake fault model. Bull. Seismol. Soc. Am. 88, 1182-1197

Massonnet, D., Rossi, M., Carmona, C., Adragna, F., Peltzer, G., Feigl, K., Rabaute, T., 1993. The displacement field of the Landers earthquake mapped by radar interferometry. Nature 364, 138-142

Mériaux, A.S., Ryerson, F.J., Tapponnier, P., Van der Woerd, J., Finkel, R.C., Xu, X., Xu, Z., Caffee, M.W., 2004. Rapid slip along the central Altyn Tagh Fault: Morphochronologic evidence from Cherchen He and Sulamu Tagh. J Geophys Res-Sol Ea 109

Mériaux, A.S., Tapponnier, P., Ryerson, F.J., Xiwei, X., King, G., Van der Woerd, J., Finkel, R.C., Haibing, L., Caffee, M.W., Zhiqin, X., Wenbin, C., 2005. The Aksay segment of the northern Altyn Tagh fault: Tectonic geomorphology, landscape evolution, and Holocene slip rate. J Geophys Res-Sol Ea 110

Mériaux, A.S., Van der Woerd, J., Tapponnier, P., Ryerson, F.J., Finkel, R.C., Lasserre, C., Xu, X., 2012. The Pingding segment of the Altyn Tagh Fault (91°E): Holocene slip-rate determination from cosmogenic radionuclide dating of offset fluvial terraces. J Geophys Res-Sol Ea 117

Molnar, P., Tapponnier, P., 1978. Active tectonics of Tibet. J Geophys Res-Sol Ea 83, 5361-5375

Nielsen, S.B., Knopoff, L., 1998. The equivalent strength of geometrical barriers to earthquakes. J Geophys Res-Sol Ea 103, 9953-9965

Oglesby, D., 2008. Rupture Termination and Jump on Parallel Offset Faults. Bull. Seismol. Soc. Am. 98, 440-447

Oglesby, D.D., Mai, P.M., 2012. Fault geometry, rupture dynamics and ground motion from potential earthquakes on the North Anatolian Fault under the Sea of Marmara. Geophys. J. Int. 188, 1071-1087

Olsen, K.B., 1997. Three-Dimensional Dynamic Simulation of the 1992 Landers Earthquake. Science 278, 834-838

Oskin, M.E., Elliott, A.J., Duan, B., Liu-Zeng, J., Liu, Z., Shao, Y., Prush, V., Morelan, A., Chester, J.S., Elizondo, D., 2015. Earthquake gates: linking rupture length to geologically constrained dynamics of fault complexity, with examples from the Altyn Tagh and San Andreas faults. Abstract presented at 2015 GSA Annual Meeting, Baltimore, Maryland, 1-4 Nov. .

Rice, J.R., 1992. Chapter 20 Fault Stress States, Pore Pressure Distributions, and the Weakness of the San Andreas Fault, in: Evans, B., Wong, T.-f. (Eds.), International Geophysics. Academic Press, pp. 475-503.

Ruina, A., 1983. Slip Instability and State Variable Friction Laws. J. Geophys. Res. 88, 359-370

Ryan, K.J., Oglesby, D.D., 2014. Dynamically modeling fault step overs using various friction laws. J Geophys Res-Sol Ea 119, 5814-5829

Scharer, K.M., Biasi, G.P., Weldon, R.J., Fumal, T.E., 2010. Quasi-periodic recurrence of large earthquakes on the southern San Andreas fault. Geology 38, 555-558

Shen, Z.-K., Wang, M., Li, Y., Jackson, D.D., Yin, A., Dong, D., Fang, P., 2001. Crustal deformation along the Altyn Tagh fault system, western China, from GPS. J Geophys Res-Sol Ea 106, 30607-30621

Shi, Z., Day, S.M., 2013. Rupture dynamics and ground motion from 3-D rough-fault simulations. 118, 1122-1141

Sibson, R.H., 1985. Stopping of earthquake ruptures at dilational fault jogs. Nature 316, 248-251

Ulrich, T., Gabriel, A.A., Ampuero, J.P., Xu, W., 2019. Dynamic viability of the 2016 Mw 7.8 Kaikoura earthquake cascade on weak crustal faults. Nat Commun 10, 1213

Wallace, K., Yin, G., Bilham, R., 2004. Inescapable slow slip on the Altyn Tagh fault. Geophys. Res. Lett. 31

Washburn, Z., Arrowsmith, J.R., Dupont-Nivet, G., Feng, W.X., Qiao, Z.Y., Zhengle, C., 2003. Paleoseismology of the Xorxol segment of the central Altyn Tagh fault, Xinjiang, China. Ann. Geophys. 46

Washburn, Z., Arrowsmith, J.R., Forman, S.L., Cowgill, E., Xiaofeng, W., Yueqiao, Z., Zhengle, C., 2001. Late Holocene earthquake history of the central Altyn Tagh fault, China. Geology 29

Wesnousky, S.G., 1988. Seismological and structural evolution of strike-slip faults. Nature 335, 340-343

Wesnousky, S.G., 2006. Predicting the endpoints of earthquake ruptures. Nature 444, 358-360

Williams, R.T., Davis, J.R., Goodwin, L.B., 2019. Do Large Earthquakes Occur at Regular Intervals Through Time? A Perspective From the Geologic Record. Geophys. Res. Lett. 46, 8074-8081

Yin, A., Rumelhart, P.E., Butler, R., Cowgill, E., Harrison, T.M., Foster, D.A., Ingersoll, R.V., Qing, Z., Xian-Qiang, Z., Xiao-Feng, W., Hanson, A., Raza, A., 2002. Tectonic history of the Altyn Tagh fault system in northern Tibet inferred from Cenozoic sedimentation. Geol. Soc. Am. Bull. 114, 1257-1295

Yuan, Z., Liu-Zeng, J., Wang, W., Weldon, R.J., Oskin, M.E., Shao, Y., Li, Z., Li, Z., Wang, P., Zhang, J., 2018. A 6000-year-long paleoseismologic record of earthquakes along the Xorkoli section of the Altyn Tagh fault, China. Earth Planet. Sci. Lett. 497, 193-203

Yue, Y., Ritts, B.D., Graham, S.A., Wooden, J.L., Gehrels, G.E., Zhang, Z., 2004. Slowing extrusion tectonics: lowered estimate of post-Early Miocene slip rate for the Altyn Tagh fault. Earth Planet. Sci. Lett. 217, 111-122

Zhu, S., Xu, C., Wen, Y., Liu, Y., 2016. Interseismic Deformation of the Altyn Tagh Fault Determined by Interferometric Synthetic Aperture Radar (InSAR) Measurements. Remote Sensing 8, 233

Prush, V.B., Oskin, M.E., Liu-Zeng, J., Shao, Y., Sion, B., personal communications. Reduction of Altyn Tagh fault slip rate through the Akatengneng Shan earthquake gate, northwest China.